

A Truncated Primordial Power Spectrum and its Impact on CMB Polarization

JINGWEI LIU¹ AND FULVIO MELIA²

¹*Department of Physics, The University of Arizona, AZ 85721, USA*

²*Department of Physics, The Applied Math Program and Department of Astronomy, The University of Arizona, AZ 85721, USA*

(Received September 6, 2024)

ABSTRACT

We investigate the impact of a hypothesized delayed initiation of inflation, characterized by a cutoff k_{\min} to the primordial power spectrum in the cosmic microwave background (CMB). This cutoff affects both the scalar and tensor spectra, which therefore impacts several measurements of the temperature and polarization distributions. We calculate the angular power spectrum and correlation function with and without k_{\min} in the context of *Planck*- Λ CDM, and demonstrate that a non-zero k_{\min} significantly improves the alignment between theory and the observations, including the temperature, E -mode polarization, TE cross-correlation, $Q+U$ polarization and $Q-U$ polarization. It creates an observable signature in both the angular power spectrum and correlation function for all cases. We thus also explore the B -mode polarization, for which current data are not yet precise enough to determine k_{\min} , but whose impact should be detectable with high-precision measurements using future missions, such as LiteBIRD, if the tensor-to-scalar ratio, r , is not much smaller than its current upper limit. We find that the introduction of k_{\min} not only addresses large-angle anomalies in the CMB but also provides a more consistent framework for understanding the early Universe's inflationary phase. These findings highlight the importance of future high-precision CMB observations in validating the existence and implications of k_{\min} .

Keywords: Cosmic inflation (319) — Cosmological models (337) — Observational cosmology (1146) — Quantum cosmology (1313)

1. INTRODUCTION

Inflation was introduced over four decades ago (Starobinskiĭ 1979; Kazanas 1980; Guth 1981; Linde 1982) to solve several major problems with standard cosmology, including an inexplicably uniform temperature in the cosmic microwave background (CMB) across causally disconnected regions of the sky, flatness (Melia 2022) and the absence of magnetic monopoles that should have been produced in large quantities in the context of grand unified theories (GUTs) (Melia 2023a). We still do not know the underlying physics of inflation, however, and very little information has been extracted thus far from the observations concerning its initiation and a possible pre-inflationary epoch.

More recently, largely due to the success of the *Planck* satellite (Planck Collaboration et al. 2020a), unprecedented

progress has been made with observations of the CMB but, contrary to expectations, inflationary theory has not been clearly confirmed. Instead, the traditional cosmological model is facing an increasing number of challenges. For example, while inflation predicts a nearly scale-invariant spectrum of primordial perturbations (Mukhanov et al. 1992), certain anomalies in the CMB—such as a lack of large-angle correlations (Copi et al. 2010), a hemispherical asymmetry (Eriksen et al. 2004) and a ‘cold’ spot (Cruz et al. 2005)—are not fully explained by standard inflationary models. Moreover, the theory itself was not established with the full compliance of General Relativity (GR) and Quantum Field Theory (QFT), so its internal structure is fragile in many ways. As a result, an increasing number of challenges to the core theory have been raised over the past few decades. Most prominently, questions have been asked concerning its initial conditions (Ijjas et al. 2013, 2014), its informal (and possibly inconsistent) handling of quantum fluctuations in the inflaton field (Martin & Brandenberger 2001) and its evident violation of the strong energy condition in GR (Melia 2023b).

The most serious concern regarding inflation is its lack of predictive power. Many efforts have been made over the years to mitigate at least some of the observational anomalies by modifying the basic model. These efforts have led to an accommodation with the data, but at the expense of increasing the model's flexibility, which also makes it difficult to falsify, since the model can easily be adjusted to fit essentially 'anything.'

Over the coming years, one of the most important observational developments related to inflation will be an attempt to measure B-mode polarization in the CMB fluctuations, believed to represent a tell-tale signature of tensor perturbations in the inflaton field (Mukhanov et al. 1992). While other mechanisms may also create such quantum fluctuations, it is understood that an absence of the signature they would leave behind in the CMB temperature profile would argue strongly against inflation having actually happened. Our focus in this paper will thus be an exploration of how k_{\min} could impact the CMB polarization signal, the E -mode part of which is already measured by *Planck* (Planck Collaboration et al. 2020a) and the B -mode part to be measured, e.g., by LiteBIRD (LiteBIRD Collaboration et al. 2023).

We take as our starting point the anomalous lack of large-angle correlations mentioned earlier, which appears to be due to a wavenumber cutoff, k_{\min} , in the primordial power spectrum (Melia & López-Corredoira 2018; Melia et al. 2021; Sanchis-Lozano et al. 2022). In so doing, however, we shall attempt to adhere as much as possible to the conventional picture of inflation, incorporated into the *Planck*- Λ CDM (standard) model. As we shall explain below, the introduction of k_{\min} is strongly motivated by the physics of the early Universe (Liu & Melia 2020; Liu & Melia 2024a). And such a cutoff is actually required by the initiation of a slow-roll inflationary phase.

We begin our discussion by briefly summarizing the basic picture of how the temperature and polarization fluctuations in the CMB are defined and how they are thought to arise from the primordial quantum fluctuations. We shall focus on two primary objectives. First, we shall discuss why polarization modes are important, and how B and E modes are defined, distinguished and used. Second, we shall elaborate upon the notion that k_{\min} corresponds to the initiation of a slow-roll inflationary expansion and how it impacts our understanding of how quantum fluctuations are generated and grown.

After this brief background, we shall explore the differences between models with and without k_{\min} , notably in their predicted angular correlation function and the corresponding angular power spectrum. We shall quantify the impact of k_{\min} on these observables, and compare the results to the existing measurements from *Planck* (Planck Collaboration et al. 2020a) and examine the likelihood of them being measured

by upcoming missions, such as LiteBIRD (LiteBIRD Collaboration et al. 2023).

2. CALCULATION OF THE ANGULAR POWER SPECTRUM AND ANGULAR CORRELATION FUNCTION

2.1. Brief Theoretical Background

Like any radiation field, the CMB can be characterized by the intensity tensor I_{ij} , from which we obtain the four well-known Stokes parameters:

$$\begin{aligned} T &= \frac{I_{11} + I_{22}}{4}, \\ Q &= \frac{I_{11} - I_{22}}{4}, \\ U &= \frac{I_{12} + I_{21}}{4}, \\ V &= \frac{I_{12} - I_{21}}{4i}. \end{aligned} \quad (1)$$

For CMB studies, only the first three of these quantities are important because Thomson scattering does not generate the V component of polarization Zaldarriaga & Seljak (1997).

We can directly use T , Q , and U to analyze the CMB, especially if we only focus on a small fraction of the sky, which can be approximated as a (local) plane. If the analysis involves large separations on the sky, however, Q and U are not appropriate because their evaluation relies on choosing a specific direction as the reference. But such a direction is not available on a sphere, which one would need to use for a large fraction of the sky. Therefore, we need to introduce the so-called B and E modes, which are rotationally independent, for the analysis of the CMB polarization (Zaldarriaga & Seljak 1997; Yoho et al. 2014). To see how these two sets of parameters are related, let us first examine the properties of Q and U .

By rotating the sky by an angle ϕ , one gets (Kosowsky 1996)

$$\begin{aligned} Q' &= Q \cos(2\phi) + U \sin(2\phi), \\ U' &= -Q \sin(2\phi) + U \cos(2\phi), \end{aligned} \quad (2)$$

which may be written more compactly as

$$(Q \pm iU)' = e^{\mp 2i\phi} (Q \pm iU). \quad (3)$$

It is therefore common to construct a pair of spin-weighted functions, $Q + iU$ and $Q - iU$, with a spin weight of 2. Notice that T is already rotation invariant, meaning it is a spin-weighted function with a spin weight of 0. Therefore, one may expand T , Q , and U in terms of spin-weighted spherical

harmonics (Zaldarriaga & Seljak 1997):

$$\begin{aligned} T &= \sum_{\ell,m} a_{T,\ell m} Y_{\ell m}, \\ Q + iU &= \sum_{\ell,m} a_{2,\ell m 2} Y_{\ell m}, \\ Q - iU &= \sum_{\ell,m} a_{-2,\ell m -2} Y_{\ell m}. \end{aligned} \quad (4)$$

The benefit of doing this is that, for spin-weighted functions, we can apply spin raising and lowering operators to transform them into spin-0 functions, which are then rotation-invariant. This step removes any ambiguity that arises from the definition of a reference direction in the sky when calculating the Q and U modes. The operation proceeds as follows (Zaldarriaga & Seljak 1997):

$$\begin{aligned} \bar{\partial}^2(Q + iU) &= \sum_{\ell,m} \left(\frac{(\ell+2)!}{(\ell-2)!} \right)^{1/2} a_{2,\ell m} Y_{\ell m}, \\ \partial^2(Q - iU) &= \sum_{\ell,m} \left(\frac{(\ell+2)!}{(\ell-2)!} \right)^{1/2} a_{-2,\ell m} Y_{\ell m}. \end{aligned} \quad (5)$$

The better known B and E modes are then defined as

$$\begin{aligned} a_{E,\ell m} &= -\frac{a_{2,\ell m} + a_{-2,\ell m}}{2}, \\ a_{B,\ell m} &= i\frac{a_{2,\ell m} - a_{-2,\ell m}}{2}, \\ E &= \sum_{\ell m} a_{E,\ell m} Y_{\ell m}, \\ B &= \sum_{\ell m} a_{B,\ell m} Y_{\ell m}. \end{aligned} \quad (6)$$

To explain how the perturbations in the CMB were generated, we adopt the synchronous gauge, in which a metric perturbation is written as (Ma & Bertschinger 1995)

$$ds^2 = a^2(\tau) \{ -d\tau^2 + (\delta_{ij} + h_{ij}) dx^i dx^j \}. \quad (7)$$

And in this framework, we introduce two fields in k -space, $h(k, \tau)$ and $\eta(k, \tau)$, such that

$$\begin{aligned} h_{ij}(x, \tau) &= \int d^3k e^{ikx} (\hat{k}_i \hat{k}_j h(k, \tau) \\ &\quad + \left(\hat{k}_i \hat{k}_j - \frac{1}{3} \delta_{ij} \right) 6\eta(k, \tau)). \end{aligned} \quad (8)$$

The scalar mode perturbations in the CMB may then be evolved according to the Boltzmann equations in the synchronous gauge as follows (Zaldarriaga & Seljak 1997; Kosowsky 1996):

$$\begin{aligned} \dot{\Delta}_T^{(S)} + ik\mu\Delta_T^{(S)} &= -\frac{1}{6}\dot{h} - \frac{1}{6}(\dot{h} + 6\eta)P_2(\mu) + \dot{\kappa} \\ &\quad - \Delta_T^{(S)} + \Delta_{T0}^{(S)} + i\mu v_b + \frac{1}{2}P_2(\mu)\Pi, \\ \dot{\Delta}_P^{(S)} + ik\mu\Delta_P^{(S)} &= \dot{\kappa} - \Delta_P^{(S)} + \frac{1}{2}[1 - P_2(\mu)]\Pi, \end{aligned} \quad (9)$$

$$\Pi = \Delta_{T2}^{(S)} + \Delta_{P2}^{(S)} + \Delta_{P0}^{(S)}. \quad (10)$$

In these expressions, $\Delta_T^{(S)}$ represents the temperature anisotropy, and a specific direction is chosen for the definition of polarization. For a given Fourier mode, the coordinate system is selected such that the wave vector k is parallel to the \hat{z} -direction. Here, μ is defined as $\hat{n} \cdot \hat{k}$, where \hat{n} denotes the direction of the photon. The Q -mode of the polarization in this coordinate system is denoted as $\Delta_P^{(S)}$, and there is no U -mode for such a coordinate.

Additional parameters include: v_b , which stands for the bulk baryon velocity, and $\dot{\kappa}$, which represents the differential optical depth and can be calculated from $\dot{\kappa} = a(\tau)n_e x_e \sigma_T$, where $a(\tau)$ is the scale factor, n_e is the electron density, x_e is the ionization fraction, and σ_T is the Thomson cross-section.

The definition of Π requires further explanation. It represents the combination of multiple moments of $\Delta_P^{(S)}$ and $\Delta_T^{(S)}$, as shown in Equation (10). The multiple moments are defined in terms of the Legendre expansion of $\Delta_P^{(S)}$ and $\Delta_T^{(S)}$, based on the general expression

$$\Delta = \sum_{\ell} (2\ell+1)(-i)^{\ell} \Delta_{\ell}(k) P_{\ell}(\mu). \quad (11)$$

To obtain the perturbations we see today, one integrates the Boltzmann equations from the last scattering surface to today along the line of sight, yielding the results (Seljak & Zaldarriaga 1996; Zaldarriaga & Seljak 1997)

$$\begin{aligned} \Delta_T^{(S)}(\tau_0, k, \mu) &= \int_0^{\tau_0} d\tau e^{ix\mu} S_T^{(S)}(k, \tau), \\ \Delta_P^{(S)}(\tau_0, k, \mu) &= \frac{3}{4}(1-\mu^2) \int_0^{\tau_0} d\tau e^{ix\mu} g(\tau) \Pi(k, \tau), \\ S_T^{(S)}(k, \tau) &= g \left[\Delta_{T,0} + 2\dot{\alpha} + \frac{v_b}{k} + \frac{\Pi}{4} + \frac{3\ddot{\Pi}}{4k^2} \right] \\ &\quad + e^{-\kappa}(\eta + \ddot{\alpha}) + \dot{g} \left[\alpha + \frac{v_b}{k} + \frac{3\dot{\Pi}}{4k^2} \right] \\ &\quad + \frac{3\ddot{g}\Pi}{4k^2}. \end{aligned} \quad (12)$$

In these expressions, we have introduced several new variables, including $x \equiv k(\tau_0 - \tau)$, where τ_0 is defined today, while τ is at the last scattering surface. Additionally, $\alpha \equiv (\dot{h} + 6\eta)/2k^2$, and $g(\tau) \equiv \dot{\kappa} \exp(-\kappa)$.

The Q -mode of polarization may be converted into the E -mode and B -mode using the spin raising and lowering operators introduced earlier. For scalar modes, the B -mode vanishes automatically, leaving only the E -mode. Then, Equation (12) becomes

$$\begin{aligned} \Delta_T^{(S)}(k) &= \int_0^{\tau_0} d\tau S_T^{(S)}(k, \tau) j_{\ell}(x), \\ \Delta_E^{(S)}(k) &= \sqrt{\frac{(l+2)!}{(l-2)!}} \int_0^{\tau_0} d\tau S_E^{(S)}(k, \tau) j_{\ell}(x), \end{aligned} \quad (13)$$

in which

$$S_E^{(S)}(k, \tau) = \frac{3g(\tau)\Pi(\tau, k)}{4x^2} \quad (14)$$

is the source term of the E -mode.

The power spectra for T and E and their cross-correlation are simply given by

$$\begin{aligned} C_{T, E \ell}^{(S)} &= (4\pi)^2 \int k^2 dk P_\phi(k) \left[\Delta_{T, E \ell}^{(S)}(k) \right]^2, \\ C_{C \ell}^{(S)} &= (4\pi)^2 \int k^2 dk P_\phi(k) \Delta_{T \ell}^{(S)}(k) \Delta_{E \ell}^{(S)}(k), \end{aligned} \quad (15)$$

in which $P_\phi(k)$ stands for the primordial power spectrum of the scalar mode. We thus see that the angular power spectrum generated by the scalar modes can be calculated by solving the set of differential Equations (10), (12), (13) and (14).

Analogously to the scalar modes, we can derive a set of differential equations for the tensor modes based on the Boltzmann equations. These are

$$\begin{aligned} \tilde{\Delta}_T^{(T)}(\tau, \mu, k) &= \int_0^\tau d\tau e^{ix\mu} S_T^{(T)}(k, \tau), \\ \tilde{\Delta}_P^{(T)}(\tau, \mu, k) &= \int_0^\tau d\tau e^{ix\mu} S_P^{(T)}(k, \tau), \end{aligned} \quad (16)$$

$$\begin{aligned} S_T^{(T)}(k, \tau) &= -\dot{h}e^{-\kappa} + g\Psi, \\ S_P^{(T)}(k, \tau) &= -g\Psi, \end{aligned} \quad (17)$$

and

$$\begin{aligned} \Psi &\equiv \left(\frac{1}{10} \tilde{\Delta}_{T0}^{(T)} + \frac{1}{7} \tilde{\Delta}_{T2}^{(T)} + \frac{3}{70} \tilde{\Delta}_{T4}^{(T)} \right. \\ &\quad \left. - \frac{3}{5} \tilde{\Delta}_{P0}^{(T)} + \frac{6}{7} \tilde{\Delta}_{P2}^{(T)} - \frac{3}{70} \tilde{\Delta}_{P4}^{(T)} \right). \end{aligned} \quad (18)$$

Combining these equations, we may solve for Ψ at any given τ . In addition,

$$\begin{aligned} \Delta_{Tl}^{(T)} &= \sqrt{\frac{(l+2)!}{(l-2)!}} \int_0^{\tau_0} d\tau S_T^{(T)}(k, \tau) \frac{j_l(x)}{x^2}, \\ \Delta_{E, Bl}^{(T)} &= \int_0^{\tau_0} d\tau S_{E, B}^{(T)}(k, \tau) j_l(x), \end{aligned} \quad (19)$$

and

$$\begin{aligned} S_E^{(T)}(k, \tau) &= g \left(\Psi - \frac{\ddot{\Psi}}{k^2} + \frac{2\Psi}{x^2} - \frac{\dot{\Psi}}{kx} \right) \\ &\quad - \dot{g} \left(\frac{2\dot{\Psi}}{k^2} + \frac{4\Psi}{kx} \right) - \frac{2\dot{g}\dot{\Psi}}{k^2}, \\ S_B^{(T)}(k, \tau) &= g \left(\frac{4\Psi}{x} + \frac{2\dot{\Psi}}{k} \right) + \dot{g} \left(\frac{2\dot{\Psi}}{k} \right). \end{aligned} \quad (20)$$

The angular power spectra are then found from the expressions (Zaldarriaga & Seljak 1997)

$$\begin{aligned} C_{Xl}^{(T)} &= (4\pi)^2 \int k^2 dk P_h(k) \left[\Delta_{Xl}^{(T)}(k) \right]^2, \\ C_{Cl}^{(T)} &= (4\pi)^2 \int k^2 dk P_h(k) \Delta_{Tl}^{(T)}(k) \Delta_{El}^{(T)}(k), \end{aligned} \quad (21)$$

in which X stands for T , E or B . Thus we can solve for Ψ from Equations (16)–(18), and then use Equations (19) and (20) to find the angular power spectrum.

Now let us briefly review how the observable fluctuations were generated from the nearly scale-free primordial spectrum, which itself was created at horizon crossing. The core concept is that, during inflation, the Universe expanded at close to an exponential rate, while the Hubble radius

$$R_H = \frac{c}{H} \quad (22)$$

remained approximately constant. The quantum fluctuation wavelengths, however, continued to grow at a rate proportional to the expansion factor, $a(t)$:

$$\lambda(k) = a \frac{2\pi}{k}. \quad (23)$$

Thus, modes that were initially smaller than R_H grew larger than the Hubble radius and left the horizon. The smaller k is (i.e., the larger the comoving wavelength), the earlier the mode crossed, satisfying the condition (Liddle 1994)

$$aH = ck. \quad (24)$$

With this conventional picture, it is easy to see why a hard cutoff k_{\min} in the primordial power spectrum should correspond to the initiation of inflation. If inflation started at a specific time, there must be a largest mode whose wavelength matches the Hubble radius at that instant. Therefore, k_{\min} serves as a strong constraint one may use to determine the time at which inflation started (Liu & Melia 2020; Liu & Melia 2024a).

Of course, the initial motivation for introducing k_{\min} was more empirical, essentially to mitigate the well-known large-angle anomalies in the CMB, confirmed by multiple observational missions, such as the Cosmic Background Explorer (COBE) (Hinshaw et al. 1996), the Wilkinson Microwave Anisotropy Probe (WMAP) (Bennett et al. 2003) and the *Planck* mission (Planck Collaboration et al. 2014, 2020a). The most significant finding of these is that the data exhibit a lack of any correlation in the temperature fluctuations on angular scales larger than about 60 degrees. A second anomaly is associated with the fact that the measured power in the temperature angular power spectrum is significantly lower than expected in the standard model at low ℓ s ($\ell \leq 4$). Several attempts have been made to mitigate this particular problem by modifying the primordial power spectrum or introducing some kind of pre-inflationary phase (Contaldi et al. 2003; Hazra et al. 2014; Schwarz et al. 2016).

The first application of a cutoff k_{\min} was to address the temperature angular correlation function (Melia & López-Corredoira 2018). This work showed that a zero k_{\min} model is ruled out at a confidence level of over 8σ . It also showed

that the angular correlation function calculated with non-zero values of k_{\min} fits the data much better than the basic standard model without the cutoff—at all angles, not just above 60 degrees. The optimized value of k_{\min} found from the analysis of $C_{TT}(\theta)$, which we shall be using for the rest of this paper, is

$$k_{\min} = (3.14 \pm 0.36) \times 10^{-4} \text{ Mpc}^{-1}. \quad (25)$$

To emphasize the significance of such a robust result, it is worth reminding ourselves of the procedure followed to achieve the 8σ confidence level. The data points in the observed angular correlation function $C(\theta)$ are highly correlated, which must thus be considered in the statistical analysis. The optimized value of k_{\min} is determined by analyzing the distribution of mock CMB catalogs, which utilize the standard cosmological model with the angular correlation function $C_{TT}(\theta)$. The uncertainty in this quantity is obtained from the r.m.s. value that encompasses 68% of the possible outcomes. This error margin is larger than what one would derive from a simple χ^2 fitting, which does not account for the correlations. Therefore, the 8σ estimate represents the most conservative limit one may adopt in the independent analysis of the angular correlation function.

Subsequent to this work, a second study with the same basic concept—that the large angle anomaly is due to a minimum k_{\min} —was carried out, though this time focusing on the angular power spectrum (Melia et al. 2021). This analysis also showed a great improvement in fitting the data at $\ell \leq 5$, with a cut-off $k_{\min} = (2.04^{+1.4}_{-0.79}) \times 10^{-4} \text{ Mpc}^{-1}$, optimized using solely the angular power spectrum rather than the angular correlation function. These two values of k_{\min} are clearly fully consistent with each other within 1σ .

We need to emphasize that, though both papers (Melia & López-Corredoira 2018; Melia et al. 2021) focused on large angle anomalies, the problems they addressed were two separate features of the CMB. The first paper focused on the temperature angular correlation function, while the second addressed the low power seen at low ℓ 's in the angular power spectrum. Also, it must be recognized that, though $k_{\min} = 0$ is ruled out at a very high level of confidence, it does not mean that the standard cosmological model itself is ruled out. It merely suggests that, to fit the data as optimally as possible, a non-zero k_{\min} must be included. One of the more important consequences of this empirical finding is that the existence of a non-zero k_{\min} points to a delayed initiation of slow-roll inflation (Liu & Melia 2020; Liu & Melia 2024a).

To make this linkage between k_{\min} and the initiation of inflation more quantitative, we shall use one of the best known slow-roll models, based on a Higgs-like potential (Bezrukov & Shaposhnikov 2008; Barvinsky et al. 2008; Lee 2018; Liu & Melia 2024a),

$$V = V_0 \left[1 - \left(\frac{\phi}{\mu} \right)^2 \right]^2, \quad (26)$$

from which we can derive the slow-roll parameters (Kolb & Turner 1994),

$$\epsilon_V \equiv \frac{M_{\text{Pl}}^2}{2} \left(\frac{V_{,\phi}}{V} \right)^2 = \frac{8M_{\text{Pl}}^2 \phi^2}{\mu^4 [1 - (\phi/\mu)^2]^2}, \quad (27)$$

and

$$\eta_V \equiv M_{\text{Pl}}^2 \frac{V_{,\phi\phi}}{V} = -\frac{4M_{\text{Pl}}^2 (\mu^2 - 3\phi^2)}{(\mu^2 - \phi^2)^2}, \quad (28)$$

where $V_{,\phi}$ denotes the first derivative of V with respect to ϕ , and $V_{,\phi\phi}$ is its second derivative. In these expressions, M_{Pl} is the reduced Planck mass, defined as $M_{\text{Pl}} = m_{\text{Pl}}/\sqrt{8\pi}$. Under the slow-roll approximation, we obtain:

$$n_s - 1 = 2\eta_V - 6\epsilon_V, \quad (29)$$

and

$$r = 16\epsilon_V. \quad (30)$$

Adopting the *Planck* measurement, $n_s = 0.966$, and the upper limit of the tensor-to-scalar ratio, $r = 0.036$ (Ade et al. 2021), we find that $\mu \approx 18.7 M_{\text{Pl}}$ and $\phi_{0.002} \approx 5.4 M_{\text{Pl}}$ (the value of ϕ at $k = 0.002 \text{ Mpc}^{-1}$). The fact that $(\phi_{0.002}/\mu)^2 \ll 1$ confirms our inference that $V(\phi)$ would have been very nearly constant at the early stage of inflation. As long as $V(\phi)$ dominated the energy density of the Universe at that point, we conclude that H must also have been approximately constant during the early stages of inflation. With slow-roll (Linde 1983),

$$\Delta_s^2 = \frac{H^2}{8\pi^2 M_{\text{Pl}}^2 \epsilon} = \frac{2H^2}{\pi^2 M_{\text{Pl}}^2 r}. \quad (31)$$

But from the definition of the amplitude, A_s , of the primordial power spectrum, we also have

$$\Delta_s^2 = A_s \left(\frac{k}{k_*} \right)^{n_s-1}, \quad (32)$$

where k_* is a pivot scale, usually taken to be 0.05 Mpc^{-1} . Thus, inserting the *Planck* measured value of the amplitude, $A_s = 2.1 \times 10^{-9}$, we conclude that $H_{\text{init}} \approx H_{0.002} = 3.1 \times 10^{37} \text{ s}^{-1}$. And, combining this with Equation (24) completely determines the initiation of inflation. From the procedure we just demonstrated, it is clear that the energy density and time at the beginning of slow-roll inflation are model-dependent. Nevertheless, it is clear how k_{\min} corresponds to the initiation time and how it plays a crucial role in constraining the cosmological model (Liu & Melia 2020; Liu & Melia 2024a).

With this conclusion, one therefore needs to modify the expressions for the angular power spectrum and polarization of the CMB temperature as follows:

$$\begin{aligned} C_{T,E\ell}^{(S)} &= 4 \int_{k_{\min}}^{\infty} dk k^2 P_{\phi}(k) \left[\Delta_{T,E\ell}^{(S)}(k) \right]^2, \\ C_{T,E,B\ell}^{(T)} &= 4 \int_{k_{\min}}^{\infty} dk k^2 P_h(k) \left[\Delta_{T,E,B\ell}^{(T)}(k) \right]^2. \end{aligned} \quad (33)$$

Clearly, k_{\min} affects all the C_ℓ 's at all ℓ 's, and therefore affects $C(\theta)$ at all angles, giving us the opportunity of confirming the existence of k_{\min} using the polarization data as well as the temperature angular power spectrum and angular correlation function. It is worth mentioning that the impact of k_{\min} on the angular power spectrum is different than that on the angular correlation function. This happens because k_{\min} is a large-scale feature, so it mainly affects the large-scale end of the power spectrum. Its impact is felt mainly on the low ℓ 's, as we shall show in the next section. In other words, it suppresses the C_ℓ values at the low ℓ 's, especially at $\ell \leq 4$. When it comes to the angular correlation function, however, every C_ℓ contributes to $C(\theta)$ at all angles, so k_{\min} 's impact is seen at all ℓ 's.

The evidence for the existence of k_{\min} provided by the temperature fluctuations in the CMB is already quite compelling (Melia & López-Corredoira 2018; Melia et al. 2021; Liu & Melia 2024b), but there are multiple reasons for delving deeper into this problem by also analyzing its impact on the polarization of the CMB.

First, there already exist some high-quality polarization data, thanks to the success of the *Planck* mission. Analyzing k_{\min} 's impact on these observations can place our analysis on firmer ground.

Second, almost all of the existing and forthcoming CMB observational campaigns are aiming to measure the CMB's polarization more precisely. If the existing or forthcoming polarization data are precise enough to tell the difference between models with and without k_{\min} , they would provide an indispensable window into the initiation time of inflation. Moreover, there is still some doubt that the large-angle anomalies represent real physics, that they are somehow a statistical 'fluke', but a strong confirmation of a non-zero k_{\min} would completely rule out that possibility.

Third and most importantly, if a non-zero k_{\min} is indeed due to a delay of the initiation of inflation, then it should not only affect the scalar primordial power spectrum but the tensor power spectrum as well, whose analysis requires the polarization data, especially the *B*-mode polarization, which can only be generated by tensor modes (or more weakly through lensing effects). Thus, the observation of *B*-mode polarization is crucial for confirming the existence of k_{\min} and improving our understanding of the early Universe.

The above discussion has summarized the theoretical motivation and procedure for calculating the angular power spectrum and angular correlation function of both the temperature fluctuations and the polarization of the CMB within the context of standard cosmology. For the remainder of this paper, most of the calculations are carried out using the CAMB code (version 1.4.0) (Lewis et al. 2000) with the most recent *Planck* results (Planck Collaboration et al. 2020a) as its default parameters. To incorporate the impact of k_{\min} , we do

not use CAMB's default primordial power spectrum. Instead, the modified primordial power spectrum used for the scalar modes is

$$P^{(S)}(k) = \begin{cases} A_s \cdot \left(\frac{k}{k_{\text{pivot}}}\right)^{n_s-1} & \text{for } k \geq k_{\min}. \end{cases} \quad (34)$$

For the tensor modes, we use

$$P^{(T)}(k) = \begin{cases} 0 & \text{for } k < k_{\min}, \\ r \cdot A_s \cdot \left(\frac{k}{k_{\text{pivot}}}\right)^{n_T} & \text{for } k \geq k_{\min}, \end{cases} \quad (35)$$

in terms of the amplitude, A_s , of the primordial power spectrum, the spectral index n_s of the scalar fluctuations, the tensor-to-scalar ratio r and the spectral index n_T of the tensor fluctuations, which we assume to be the conventional $n_T = -r/8$ and the pivot scale $k_{\text{pivot}} = 0.05 \text{ Mpc}^{-1}$. The value of k_{\min} is given in Equation (25). The rest of the parameters are derived from the most recent *Planck* results.

For the angular correlation function, the calculation of the *E*-mode self-correlation, *TE* cross-correlation, and the *B*-mode self-correlation, are performed using our own code. In contrast, the calculation of the temperature self-correlation, and the *Q+U* and *Q-U* modes' self-correlations, is carried out using CAMB.

2.2. Analysis of the Temperature Signal

We shall begin our analysis with the TT angular power spectrum and the corresponding angular correlation function. These have already been published (Melia & López-Corredoira 2018; Melia et al. 2021), but our reason for reproducing these results is to confirm the reliability of our method before progressing to the more important polarization features.

The angular power spectrum C_ℓ^{TT} shown in Figure 1 was calculated using the CAMB code with the setup we described above. We can clearly see the low power anomaly in this figure, especially for $\ell = 2$ and $\ell = 4$, where the values measured by *Planck* (Planck Collaboration et al. 2020a) are significantly below the values predicted by the standard model with $k_{\min} = 0$, even falling outside the 1σ region of the measurement. However, once we introduce k_{\min} into the analysis, the predicted values align much more closely with the measured ones. We want to emphasize that the two theoretical curves shown here are not fitted to the *Planck* data. They are directly calculated with CAMB using the most recent cosmological parameters optimized by *Planck* (Planck Collaboration et al. 2020a). Another important observation from this figure is that k_{\min} does not affect the angular power spectrum at $\ell > 5$. In this range, the two theoretical curves are identical. In other words, for the TT angular power spectrum, introducing k_{\min} helps explain the lack of large-angle

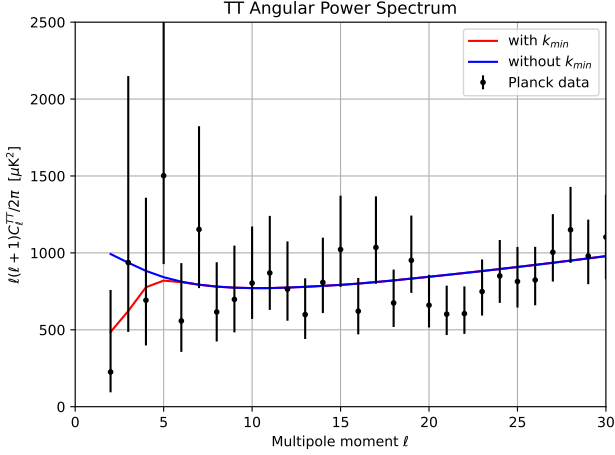


Figure 1. Lensed TT angular power spectrum with tensor modes, for multipoles $\ell \leq 30$. The blue curve includes the effects of k_{\min} , while the red curve represents the standard model's prediction without k_{\min} . The *Planck*-2018 data points with error bars are shown in black.

correlation anomaly, but does not harm the part of the angular power spectrum that was performing very well in terms of fitting the data with the standard model.

Throughout this paper, the value of k_{\min} we use is obtained from the optimization of the TT angular correlation function. Therefore, in terms of statistical analysis, we focus on the angular correlation functions. While we include the angular power spectrum plots for completeness, a quantitative comparison between models is performed only for the angular correlation functions.

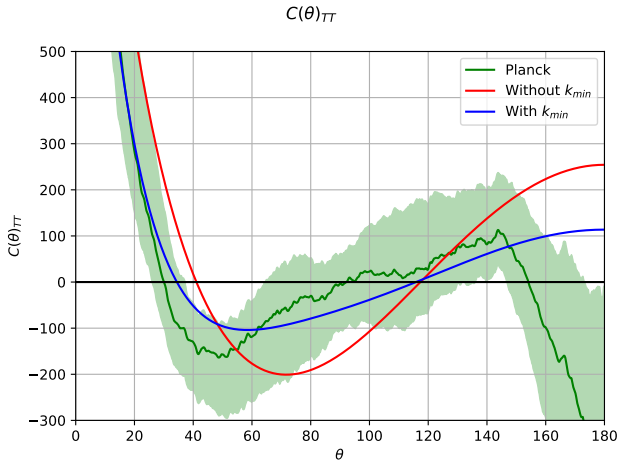


Figure 2. TT angular correlation function with (blue) and without (red) k_{\min} , in comparison with the angular correlation function calculated from the *Planck* data (green). The shaded region represents the (non-Gaussian) 1σ uncertainty obtained from a sample of three thousand mock correlation functions generated via Monte Carlo randomization.

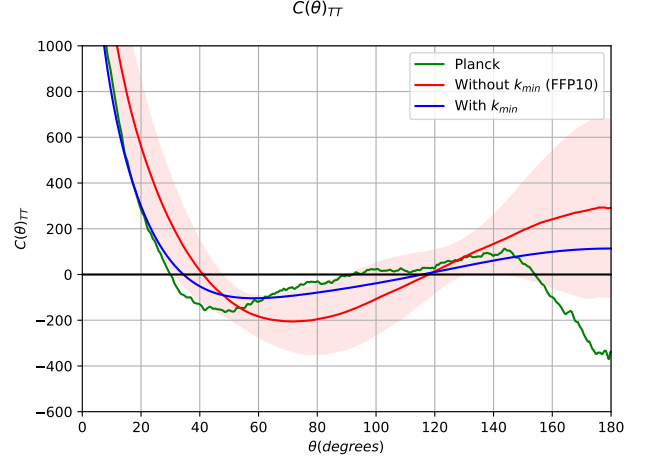


Figure 3. Same as Fig. 2, except that here the shaded region (red) corresponds to the 1σ cosmic variance, calculated utilizing *Planck*'s official set of simulations (FFP10) for the concordance model (red curve).

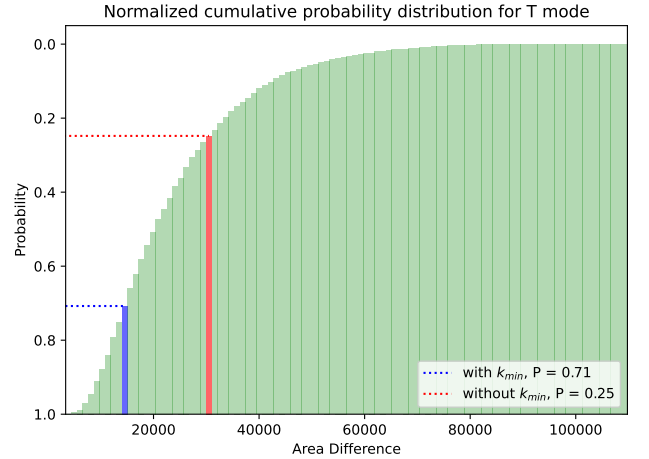


Figure 4. The cumulative probability distribution of the temperature mode, generated from the area differences between the *Planck* curve and the three thousand realizations produced using *Planck*'s total errors. Blue represents the model with k_{\min} ; red represents the model without k_{\min} .

The TT angular correlation function is shown in Figures 2 and 3. In Figure 2, we display the two theoretical curves with and without k_{\min} , calculated with CAMB using the angular power spectrum in Figure 1. The *Planck* curve was also calculated with CAMB using the power spectrum data in Figure 1. In addition, Figure 2 includes the 1σ uncertainty associated with the *Planck* curve, achieved by generating three thousand mock realizations of the angular correlation function. Specifically, for each ℓ , we used the measured value of C_ℓ^{TT} and its corresponding errors to generate a mock sample of this C_ℓ^{TT} . To address the non-Gaussianity of the data, we assumed that the upper and lower errors of C_ℓ^{TT} satisfy

two different half-Gaussian distributions, and then randomized the C_ℓ^{TT} values within these distributions. This process yielded a complete mock set of C_ℓ^{TT} , from which we calculated a mock $C(\theta)$ curve. We repeated this process three thousand times to generate three thousand mock $C(\theta)$ curves, and then determined the 1σ range of $C(\theta)$ at every angle using these samples. To properly address the non-Gaussianity (because these $C(\theta)$ samples were generated from non-Gaussian distributions, they obviously carry non-Gaussianity), we assumed that the upper and lower errors of $C(\theta)$ at every angle satisfy two different half-Gaussian distributions. In other words, the 1σ region was calculated separately for the upper and lower errors.

From Figure 2, we can clearly see the lack of large-angle correlations in the data. The theoretical curve without k_{\min} misses the *Planck* curve at all angles and even falls outside of the 1σ error region over some of the plot. This situation is notably worse than the deficit of power at low ℓ 's seen in the angular power spectrum. This is because (as noted earlier) every C_ℓ contributes at all angles. Thus, the discrepancy between measured and theoretical C_ℓ values (which only appears at low ℓ 's) is observed at all angles in the angular correlation function. After introducing k_{\min} , we see that the theoretical curve aligns much more consistently with the measured curve—at all angles. The cutoff k_{\min} not only improves the performance of the theoretical curve at angles > 60 degrees, but actually also enhances the fit at < 60 degrees. After introducing k_{\min} , the theoretical curve falls within the 1σ error region throughout the plot.

The TT angular correlation function is shown again in Figure 3, but this time with an alternative method of analysis. This time, the 1σ region corresponds to the theoretical curve without k_{\min} , based solely on cosmic variance, estimated using the *Planck* official simulations (FFP10 CMB realizations). Specifically, we took a thousand simulated CMB maps from the FFP10 (Planck Collaboration et al. 2020a) simulation, used Healpy (Gorski et al. 2005) to read these maps, and calculated their angular power spectrum. We then used CAMB to calculate their angular correlation function. The samples we used only included the cosmic variance as the source of error, which is assumed to be Gaussian. The theoretical curve without k_{\min} and the corresponding 1σ region were then calculated, respectively, by taking the average and the uncertainty of these one thousand samples at each angle. The theoretical curve with k_{\min} is the same as the one shown in Figure 2. Figure 3 also shows that introducing a non-zero k_{\min} significantly improves the consistency between the observations and theoretical predictions.

This visual comparison showing that the introduction of k_{\min} significantly improves the alignment between the model and the measurements may be made more quantitative, as described below. Notably, we shall compare three curves:

two generated from theoretical predictions and one derived from measurements. Statistical tests based on how well one curve matches another tend to be based on area differences. We shall adopt a technique introduced for such situations in Melia & Yennapureddy (2018).

Specifically, we calculate the area difference between the *Planck* curve and the 3,000 realizations used to estimate its 1σ region. We then compute and plot the cumulative probability distribution, shown in Figure 4. This figure actually represents the cumulative frequency of the three thousand realizations versus the area difference, divided into 100 bins. It allows us to estimate the probability that a given area difference arises from the total errors of the measurements, which were used to generate the three thousand realizations.

We then calculate the area differences between the two theoretical curves and the *Planck* curve. Next, we identify the corresponding bins on the cumulative probability distribution plot, and estimate the probability that the area difference between a theoretical curve and the *Planck* curve arises solely from the total error of the *Planck* measurements. The results show that, for the theoretical curve without k_{\min} , the probability that the area difference is due to the total errors of the *Planck* measurements is 0.25. For the curve with k_{\min} , the probability is 0.71. These results clearly indicate that introducing k_{\min} significantly reduces the discrepancy between theory and observation.

The analysis and results we have presented here confirm those obtained by the previously published work which, however, used a different method of analysis and a different set of data (*Planck*-2014). Introducing k_{\min} has significantly brought the theoretical predictions closer to the measurements at the low ℓ end of the angular power spectrum and at all angles of the angular correlation function.

2.3. Analysis of the E-Mode Polarization

Let us now proceed to an analysis of the *E*-mode polarization. Again, we calculate the *E*-mode angular power spectrum and the angular correlation function. It is important to note that when calculating the *E*-mode polarization, both the scalar and tensor modes contribute to the final results, which are also impacted by lensing effects. We use CAMB and *Planck*'s optimized parameters (Planck Collaboration et al. 2020a) to calculate these *E*-mode quantities. For the spectral index n_T of the tensor fluctuations, we employ the conventional assumption that $n_T = -r/8$. For the tensor-to-scalar ratio r , we initially compare the outcomes for two different values, $r = 0.00461$ and $r = 0.036$. We choose $r = 0.036$ because it represents the current upper limit from the analysis of the *Planck* and BICEP2/Keck data (Tristram et al. 2021). We choose $r = 0.00461$ to be consistent with the *B*-mode analysis that we shall motivate later. As it turns out, the angular power spectra resulting from this procedure are extremely

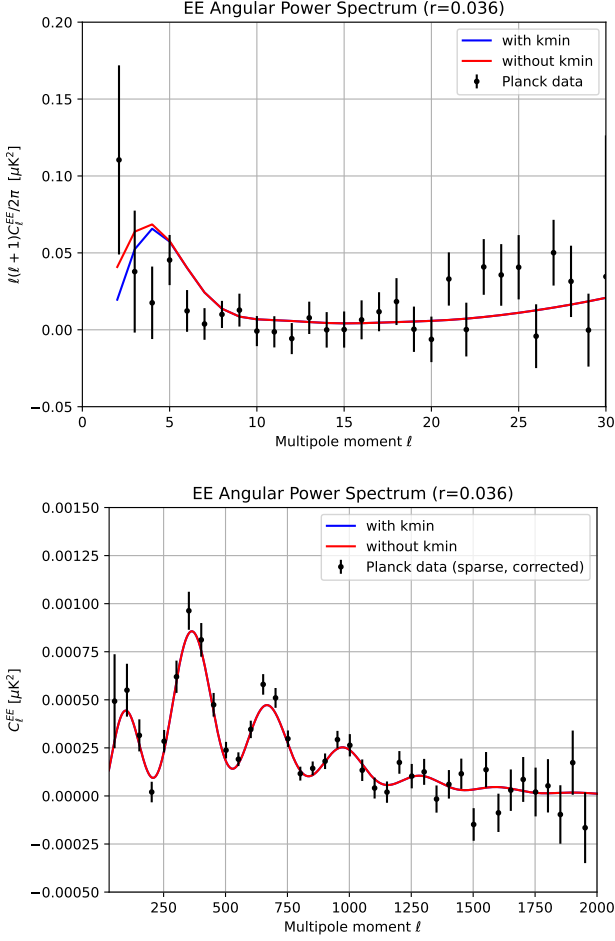


Figure 5. Lensed power spectra with tensor modes. Top: the EE power spectrum for multipoles $\ell \leq 30$. Bottom: the EE power spectrum for multipoles $\ell > 30$. In both cases, the blue curve includes the effects of k_{\min} , while the red curve represents calculations without it, i.e., the conventional application of the standard model. The *Planck*-2018 data points with error bars are shown in black.

similar in spite of the different r values, presumably because the E -modes are predominantly sourced by scalar rather than tensor perturbations. For the following analysis, we therefore retain only the results corresponding to $r = 0.036$.

The angular power spectrum C_ℓ^{EE} is shown in Figure 5. One can easily confirm that (i) the low power anomaly not only appears in the temperature angular power spectrum, but is also evident here, for $\ell < 7$; (ii) the theoretical prediction is always greater than the measured values, except for $\ell = 2$. It is worth noting, however, that *Planck*'s MC simulations are not able to quantify the residual systematics at $\ell = 2$ (*Planck Collaboration et al. 2020b*); (iii) similarly to the situation with the temperature angular power spectrum, k_{\min} helps to lower the power at low ℓ 's. The improvement, however, is not as significant as in the temperature case. After introducing k_{\min} , the predicted values are still somewhat

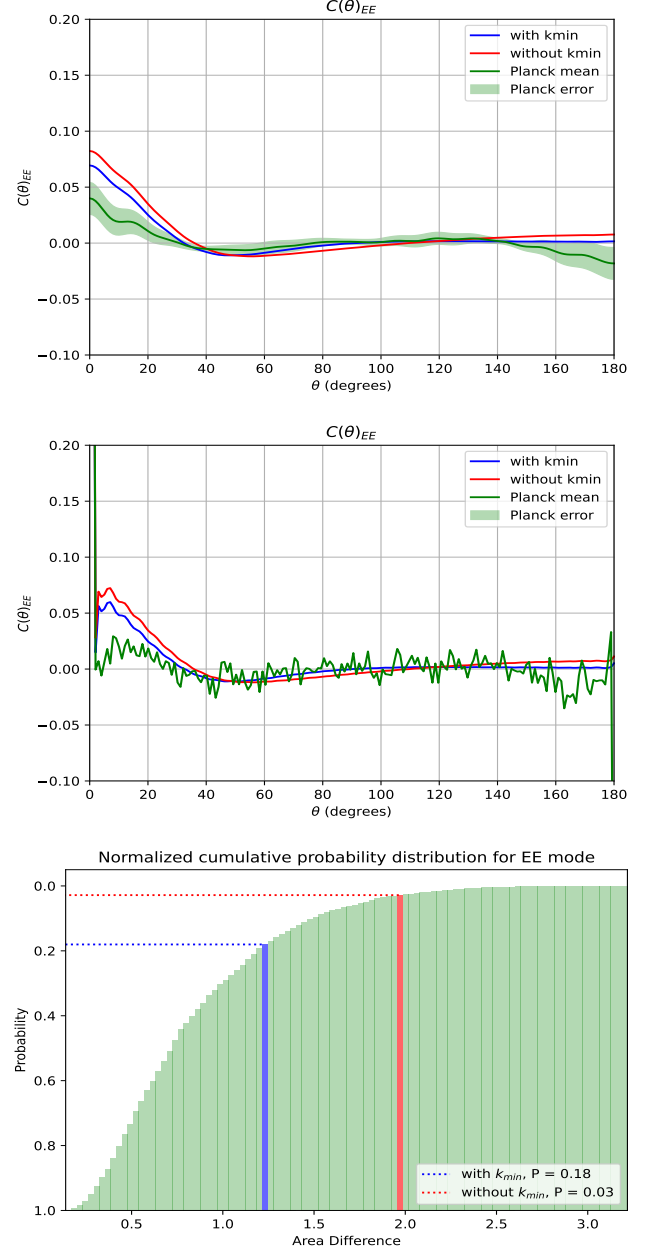


Figure 6. EE angular correlation function. Top: the EE angular correlation functions including $\ell \leq 30$ modes. Middle: the EE angular correlation functions including $\ell \leq 1500$ modes. In both cases, the blue curve includes the effects of k_{\min} , while the red curve represents the conventional application of the standard model without k_{\min} . The green curve represents the angular correlation function calculated from the *Planck*-2018 data. The corresponding 1σ region was generated from a three thousand step MC simulation utilizing the total errors in *Planck*'s measurements. Bottom: The cumulative probability distribution of the EE mode (including $\ell \leq 30$ modes only), generated from the area differences between the *Planck* curve and the three thousand realizations mentioned above, which were produced using *Planck*'s total errors. Blue represents the model with k_{\min} ; red represents the model without k_{\min} .

higher than the measured ones; and (iv) another important result of this calculation is that the two theoretical curves (with and without k_{\min}) are extremely similar at $\ell > 5$, indicating that, while k_{\min} helps resolve the low power anomaly at low ℓ 's, it does not affect the success of the conventional models at high ℓ 's.

Calculation of the angular correlation function from the angular power spectrum is straightforward, given that (Bauermann & Zaldarriaga 2009)

$$\begin{aligned} C_{EE}(\theta) &= \sum_{\ell} \frac{2\ell+1}{4\pi} C_{\ell}^{EE} P_{\ell}(\cos \theta), \\ C_{BB}(\theta) &= \sum_{\ell} \frac{2\ell+1}{4\pi} C_{\ell}^{BB} P_{\ell}(\cos \theta). \end{aligned} \quad (36)$$

The results are shown in Figure 6, which shows the EE self-angular correlation function calculated from the angular power spectrum in Figure 5. The results of models with and without k_{\min} correspond to blue and red, respectively. The *Planck* measurements are plotted in green, along with their 1σ error regions, calculated from *Planck*'s published EE angular power spectrum data (Planck Collaboration et al. 2020a) through a three thousand step Monte Carlo (MC) simulation. To be more specific, we took the observed values of the EE angular power spectrum and their errors (which were published as Gaussian errors), and then generated three thousand sets of mock C_{ℓ}^{EE} 's. An angular correlation function was calculated for each set, and from these we then determined the average and standard deviation of the angular correlation function at each angle.

We performed this analysis for the range $\ell \leq 30$ because, as observed from the angular power spectrum of the *E*-mode polarization, the impact of k_{\min} is significant only at $\ell < 6$. Additionally, including higher ℓ terms makes the angular correlation function fuzzy because high- ℓ Legendre polynomials oscillate significantly with respect to angle. Therefore, we believe that including only a limited range of ℓ 's is beneficial for demonstrating the impact of k_{\min} on the angular correlation function. We also present the results for $\ell \leq 1500$ here (middle panel of Figure 6) to make our results more complete and to support the above conclusion. As we can see from the plot, the trend of the three curves is very similar to the $\ell \leq 30$ case. However, the *Planck* curve appears fuzzy and appears to be unstable at very small and large angles (close to 0 and 180 degrees). Therefore, the quantitative analysis will be performed on the $\ell \leq 30$ case. For the rest of this paper, we shall always limit the range to $\ell \leq 30$ for the analysis of the angular correlation function associated with the *E* mode.

As we can see from the EE angular correlation plots, the conventional model without k_{\min} does not fit the observed data at all. Similarly to the temperature case, it is too large at $\theta < 40^\circ$, too small at $60^\circ < \theta < 120^\circ$, and too large again at $\theta > 140^\circ$. On the $\ell < 30$ plot, it even misses the 1σ error

region at most angles. After introducing k_{\min} , the theoretical curve is significantly closer to the observed one. Although it is still too large at $\theta < 30^\circ$, it fits the observed curve very well at $60^\circ < \theta < 120^\circ$; more importantly, it lies within the 1σ error region of the observed curve at most angles.

Similar to the case of the *TT* angular correlation functions, we are comparing three curves: two from theoretical predictions and one calculated from measurements. To quantitatively assess differences between these curves, we again use a cumulative probability approach to estimate the likelihood that the area difference between a theoretical curve and the *Planck* curve arises solely from the total errors of the *Planck* measurements. The results are shown in the bottom panel of Figure 6. For the theoretical curve without k_{\min} , the probability that the area difference is due to the total errors of *Planck* is 0.03. For the curve with k_{\min} , the probability is a much improved 0.18.

It is very clear from the analysis of the EE angular power spectrum and angular correlation function that we confirm the results of previous work based on the CMB temperature. Introducing k_{\min} significantly helps in bringing the theoretical predictions closer to the observed results. It is worth noting, however, that although the analysis of the *E*-mode makes the conclusion more robust with the inclusion of polarization data, the *E*-mode is still dominated by scalar perturbations. As mentioned earlier, if k_{\min} truly exists and is due to the onset of slow-roll inflation, it should impact not only the scalar but tensor modes as well. We shall thus analyze the *B*-mode polarization shortly.

2.4. Analysis of the *TE* Cross Correlation

We next consider the *TE* cross-correlation between the temperature and *E*-mode polarization in the CMB. This cross-correlation provides substantial information about the reionization era. Analyzing the *TE* mode is essential for breaking the degeneracies between various cosmological parameters, thereby leading to more precise measurements. Furthermore, the *TE* mode serves as an instrumental tool for testing cosmological models, as it offers an independent check of the results obtained from the temperature and *E*-mode polarization power spectra separately.

Again, we will begin our analysis with the angular power spectrum of the *TE* mode, and then move on to the angular correlation function. When calculating the *TE* cross-correlation, both scalar and tensor modes contribute to the final result, and is also influenced by the lensing effect. We use CAMB along with *Planck*'s optimized parameters (Planck Collaboration et al. 2020a) to calculate the angular power spectrum. Similarly to the *E*-mode case, we adopt the conventional assumption that $n_T = -r/8$. The tensor-to-scalar ratio $r = 0.036$ is chosen to be consistent with the analysis focusing solely on *E*-mode.

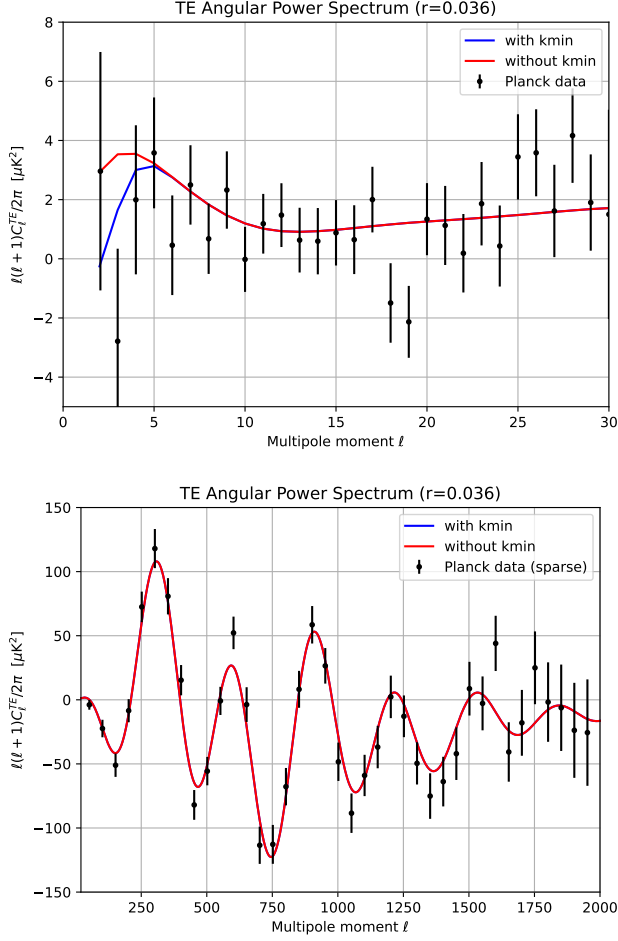


Figure 7. *TE* Lensed power spectra with tensor modes. Top: the *TE* power spectrum for multipoles $\ell \leq 30$. Bottom: the *TE* power spectrum for multipoles $\ell > 30$. In both cases, the blue curve includes the effects of a minimum wavenumber k_{\min} , while the red curve represents calculations without it, i.e., the conventional application of the standard model. The *Planck*-2018 data points with error bars are shown in black.

The results of the angular power spectrum are shown in Figure 7. The top panel displays the low ℓ region ($\ell \leq 30$), while the bottom panel shows the rest ($30 < \ell < 2000$). In both plots, the blue curve includes the effects of a minimum wavenumber k_{\min} , while the red curve represents calculations without k_{\min} . Additionally, the most updated *Planck* data are presented along with their errors in black.

The first observation one can make from an inspection of these plots is that the low power anomaly at low ℓ 's in the angular power spectrum is very apparent. Though the error bars for the first few ℓ 's are quite large, the downward trend in the power spectrum is very pronounced, and is much steeper than the theoretical curve without k_{\min} . The $\ell = 2$ mode appears to be an exception; however, as mentioned earlier, *Planck*'s MC simulations cannot quantify the residual systematics at $\ell = 2$.

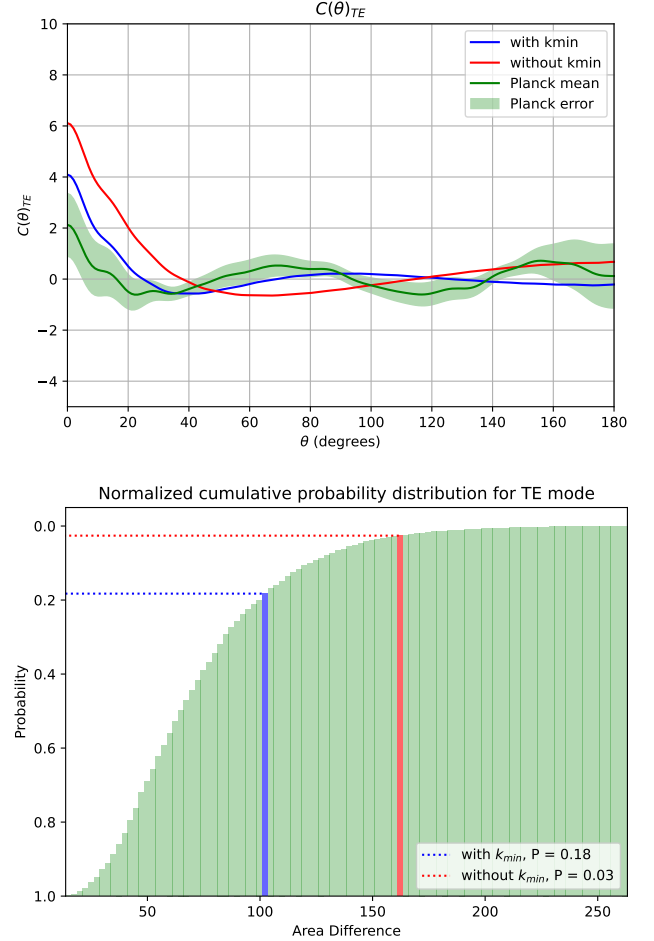


Figure 8. *TE* angular correlation function. Top: the *TE* angular correlation function including $\ell \leq 30$ modes. The blue curve includes the effects of k_{\min} , while the red curve represents calculations without k_{\min} , i.e., the conventional application of the standard model. The green curve represents the angular correlation function calculated from the *Planck*-2018 data. The corresponding 1σ region was generated from a three thousand step MC simulation utilizing the total errors in *Planck*'s measurements. Bottom: The cumulative probability distribution of the *TE* mode, generated from the area differences between the *Planck* curve and the three thousand realizations mentioned above, which were produced using *Planck*'s total errors. Blue represents the model with k_{\min} , red represents the model without k_{\min} .

A second observation is that, similarly to the temperature case, there is an obvious difference at $\ell < 6$ between the theoretical curves with and without k_{\min} . The curve with the cutoff is obviously steeper and fits the data much better, though at $\ell = 3$, the prediction still falls outside the 1σ error region. This feature in C_{ℓ}^{TE} is more pronounced than in C_{ℓ}^{EE} . Third, there is almost no difference between the two theoretical curves at $\ell > 6$, as was the case for the temperature and *E*-mode polarization.

The equation used to calculate the TE cross-correlation function is (Baumann & Zaldarriaga 2009)

$$C_{TE}(\theta) = \sum_{\ell} \frac{2\ell+1}{4\pi} C_{\ell}^{TE} P_{\ell}(\cos \theta). \quad (37)$$

To ensure consistency with the E -mode analysis, we select the range of ℓ for our calculations to be $\ell \leq 30$. The results for the models, both with and without k_{\min} , are obtained using Equation (37) with the TE angular power spectrum computed via CAMB, based on the latest *Planck* optimized parameters (Planck Collaboration et al. 2020a), and are plotted in Figure 7. The *Planck* curve and its 1σ confidence region are derived from *Planck*'s published TE angular power spectrum data through a three-thousand step Monte Carlo (MC) simulation. We utilize the observed values of the TE angular power spectrum and their reported Gaussian errors to generate three thousand mock sets of C_{ℓ}^{TE} . An angular correlation function is then calculated for each mock set, and we compute the mean and standard deviation of the angular correlation functions at each angle.

Our results are shown in Figure 8. The theoretical prediction without k_{\min} is displayed in red, while the case with k_{\min} is shown in blue. The curve calculated from *Planck*'s measurements is presented in green, along with its 1σ error region. Unlike the temperature case, there is no lack of large-angle correlation, but the theoretical prediction without k_{\min} still deviates significantly from the measurements at almost all angles, crossing into the 1σ region in only a few limited areas. After introducing k_{\min} , however, the theoretical fit improves significantly at most angles, bringing it much closer to the measurements.

Again, we quantitatively compare the fits using a cumulative probability approach to estimate the probability that the area difference between a theoretical curve and the *Planck* curve arises solely from the total errors in *Planck*. The results are shown in the bottom panel of Figure 8. For the theoretical curve without k_{\min} , the probability that the area difference is due to the total errors of the *Planck* measurements is 0.03. For the curve with k_{\min} , the probability is a much improved 0.18.

The results obtained from the TE angular power spectrum and cross-correlation function clearly confirm the conclusions drawn by the previous study based solely on the temperature, and also with the earlier analysis in this paper, i.e., the low power anomaly is quite pronounced in the TE angular power spectrum. Introducing k_{\min} to the conventional model significantly helps to align the theoretically predicted curve with the observations, and has no impact on the predictions at $\ell > 6$, where the conventional model is already very successful. The difference between the cases with and without k_{\min} is definitely detectable, and the data clearly favor the model with k_{\min} . And though there is no lack of large-angle corre-

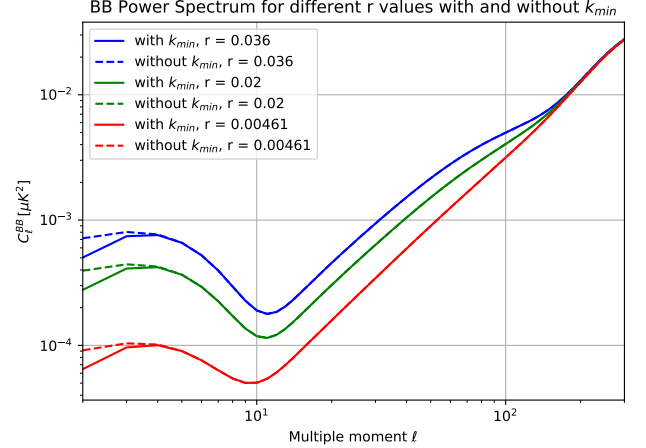


Figure 9. BB angular power spectrum for different values of r : 0.00461, 0.02 and 0.036, with (solid) and without (dashed) k_{\min} .

lation in the TE cross-correlation plots, the theoretically predicted TE angular correlation function deviates significantly from the measurements, while introducing k_{\min} helps to ease the tension considerably.

2.5. Analysis of the B -mode Polarization

Parts of the B -mode results we present here have been included in one of our previous papers (Liu & Melia 2024b). However, to make the discussion here self-contained, we shall present the complete analysis.

A study of the B -mode polarization is quite different from the E -mode and the cross-correlations. On the one hand, because B -mode can only be generated from tensor modes or through the lensing effect (Zaldarriaga & Seljak 1997; Zaldarriaga & Seljak 1998; Lewis & Challinor 2006), which transforms part of the E -mode polarization into B -mode, it is very sensitive to the tensor-to-scalar ratio r . Unfortunately, there is no definitive way to constrain this parameter very well; we only have an estimated upper limit, which comes from the cross-analysis of *Planck* and BICEP2/KECK data (Tristram et al. 2021), giving us the value $r < 0.036$. Therefore, in our analysis, we will try different values of r . As we shall show later, the larger the value of r , the more pronounced is the difference we can observe between the cases with and without k_{\min} . On the other hand, there is currently no solid observational data for B -mode, so the theoretical predictions have no firm constraints at the moment. Thus, we shall use the predicted accuracy of the upcoming LiteBIRD (LiteBIRD Collaboration et al. 2023) mission as a reference to determine under what circumstances the differences between the cases with and without k_{\min} are measurable with the next generation of CMB detectors.

Figure 9 shows how the angular power spectrum of the B -mode polarization is affected by the tensor-to-scalar ratio r . In this figure, we have plotted both cases with and without

k_{\min} , for three different values of r . These values are chosen for the following reasons: $r = 0.036$ is the current upper limit which, as we shall demonstrate, offers the largest opportunity to detect the difference between the cases with and without k_{\min} ; $r = 0.00461$ is the value used by the LiteBIRD team when presenting their predictions of the observatory's accuracy; and as we shall see, $r = 0.02$ is the value for which the difference in angular power spectra first becomes detectable. It is quite evident that the larger the tensor-to-scalar ratio, the larger is the angular power spectrum at $\ell < 200$. Noting that this is a log-log plot, it is also very clear that the larger the tensor-to-scalar ratio, the more pronounced is the difference between the cases with and without k_{\min} .

The manner in which the tensor-to-scalar ratio r affects the B -mode angular power spectrum is linked to how B -mode polarization is generated. As mentioned earlier, B -mode arises from tensor fluctuations and the lensing effect. While tensor modes primarily induce B -mode at large scales, the lensing effect mainly induces B -mode at small scales because gravitational lensing occurs locally in regions that are tiny compared to the entire sky. As a result, tensor modes mainly contribute to the low ℓ end of the spectrum, while the lensing effect contributes to the high ℓ end.

As we can see from Figure 9, similarly to the temperature and E -mode cases, the impact of k_{\min} is primarily observed in the range $\ell \leq 4$. Therefore, we have magnified this portion of the BB angular power spectrum in Figure 10 to highlight the impact of k_{\min} and compare it to the accuracy of the LiteBIRD mission. Figure 10 was produced through Monte Carlo (MC) simulations. We took the theoretically predicted values of C_ℓ 's (which we show in Figure 9) and the predicted error bars (total errors) of the LiteBIRD mission (LiteBIRD Collaboration et al. 2023), expected to provide the most sensitive B -mode measurement, together with an assumption that these errors are Gaussian (as presented in LiteBIRD's publications). We then randomized the values of the predicted C_ℓ 's based on these errors, and subsequently calculated the average and the uncertainty at each ℓ .

From Figure 10, we can easily see how the tensor-to-scalar ratio r will affect the detection of k_{\min} . For $r = 0.00461$, it is almost impossible to distinguish between the two theoretical curves as they are completely submerged within each other's 1σ region. For $r = 0.02$ and $r = 0.036$, the two cases can be distinguished at $\ell = 2$ and can be barely distinguished at $\ell = 3$. At $\ell \geq 4$, they are not distinguishable. Since 0.036 is already the upper limit of r , we are not optimistic about the detection of k_{\min} in the B -mode angular power spectrum. However, this also means that even if upcoming missions such as LiteBIRD do not observe any low ℓ anomalies as seen in the temperature data, it does not necessarily mean that k_{\min} does not exist, especially if the upper limit of r is constrained to smaller values as more accurate measurements become available.

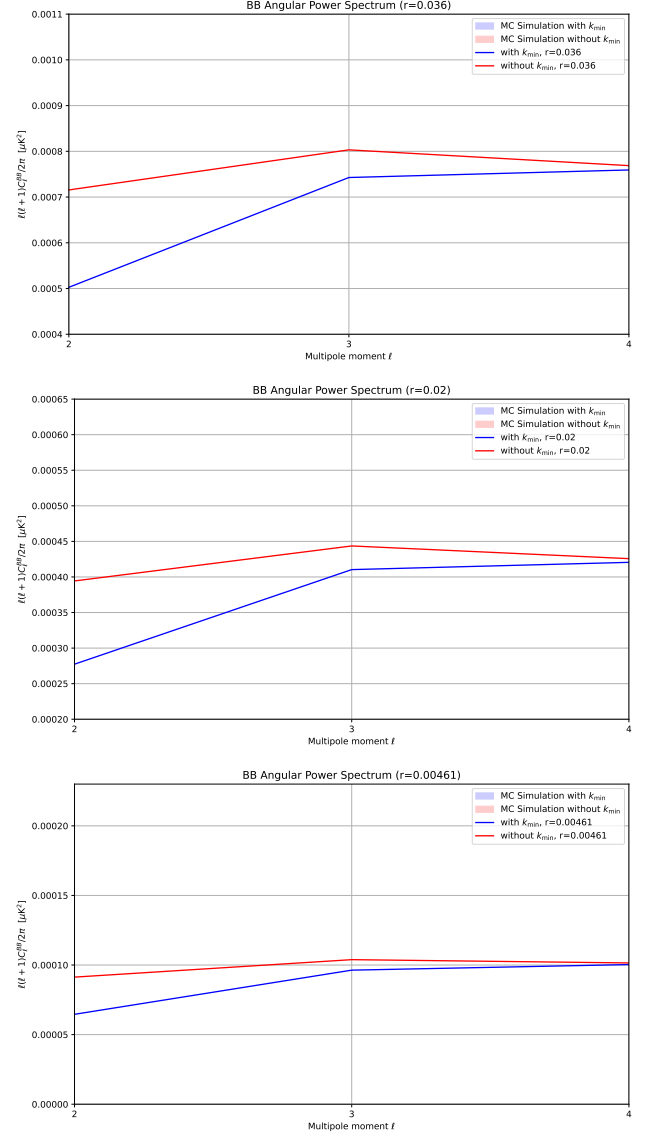


Figure 10. BB angular power spectrum for $\ell \leq 4$. In all three panels, the blue and red lines show the results with and without k_{\min} . The shaded regions represent the expected total LiteBIRD errors, including foreground residuals. The top panel is for $r = 0.036$, including the forecast $\pm 1\sigma$ region; the middle panel is for $r = 0.02$, with the expected $\pm 1\sigma$ region; the bottom panel is for $r = 0.00461$, with the forecast $\pm 1\sigma$ region.

As was the case for the angular power spectrum, we shall calculate the B -mode angular correlation function for three different r values: $r = 0.036$, $r = 0.02$, and $r = 0.00461$. And similarly to the E -mode analysis, we use Equation (36) to directly calculate the B -mode angular correlation function, whose results are shown in Figure 11.

The three plots in this figure correspond to the three different values of r . In all three panels, the blue and red curves show the results with and without k_{\min} . The shaded regions represent the predicted 1σ errors, which correspond to Lite-

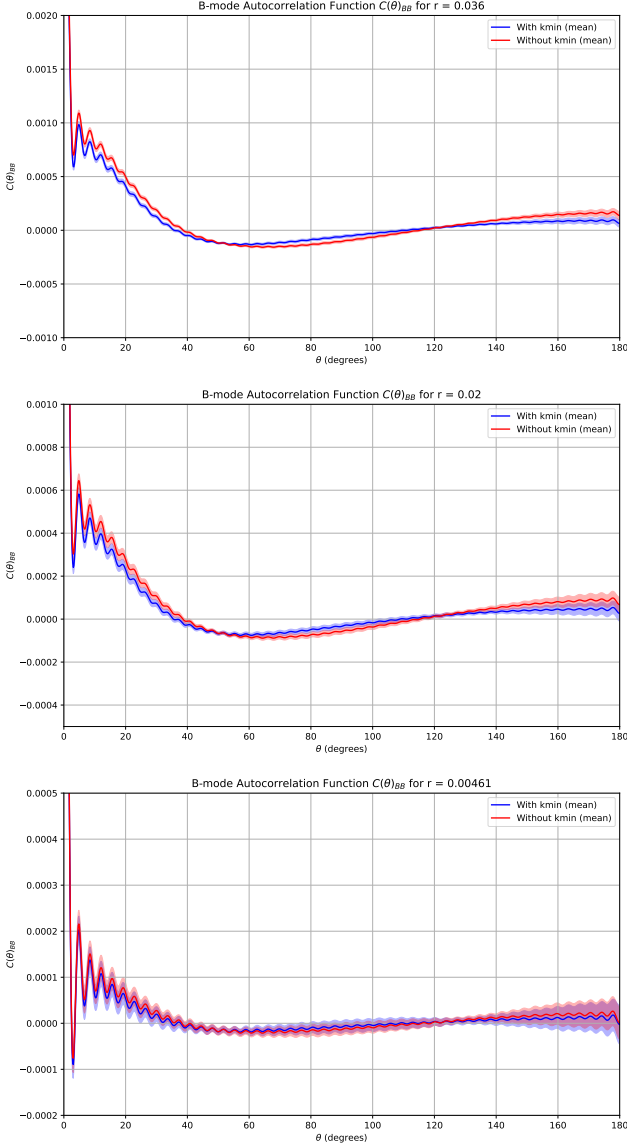


Figure 11. BB angular correlation function including $\ell < 100$ modes. In all three panels, the blue and red lines show the results with and without k_{\min} and the corresponding 1σ region was generated via a MC simulation utilizing the predicted LiteBIRD’s total errors. The top panel is for $r = 0.036$, including the forecast $\pm 1\sigma$ region; the middle panel is for $r = 0.02$, with the expected $\pm 1\sigma$ region; the bottom panel is for $r = 0.00461$, with the forecast $\pm 1\sigma$ region.

BIRD’s predicted total errors. The method we use to create these plots is similar to that applied to the E -mode analysis. We take the theoretically predicted C_{ℓ}^{BB} ’s of the different cases (with and without k_{\min} for different values of r), and then run a one thousand-step MC simulation on each of these sets. To be more specific, we randomize these six sets of C_{ℓ}^{BB} ’s according to LiteBIRD’s predicted total errors. For each simulation, we calculate the angular correlation func-

tion, limiting our analysis to a certain range of ℓ ’s ($\ell < 100$) for two reasons. First, similarly to the E -mode case, including high ℓ terms makes the angular correlation function fuzzy. More importantly, on the angular power spectrum plots, the differences between the cases with and without k_{\min} are only apparent at very low ℓ ’s, such as $\ell \leq 5$. Second, LiteBIRD provided total error predictions only for a limited range of ℓ ’s ($\ell < 200$). We then calculate the average and standard deviation for each of the six cases individually at all angles. On the plots, the theoretical curves represent the calculated averages, and the 1σ regions represent the standard deviations.

The results shown in Figure 11 are quite interesting. For the $r = 0.00461$ case, the conclusion is similar to that of the angular power spectrum, where the difference between the cases with and without k_{\min} is too small at all angles, and the two theoretical curves are well within each other’s 1σ region for most of the angles. For the other two values of r , however, the situation is quite different. In the angular power spectrum analysis, we concluded that even for $r = 0.036$, where we observe the largest separation between the two cases, the difference is barely identifiable at $\ell = 3$ and is only obvious at $\ell = 2$. However, in the angular correlation function, for $r = 0.036$, we can clearly see a distinct difference between the cases with and without k_{\min} at all angles, especially for $\theta < 120^\circ$, where the two curves are far outside each other’s 1σ region. For the $r = 0.02$ case, the two curves are outside each other’s 1σ region at most angles. Therefore, we believe that in terms of detecting k_{\min} in the B -mode polarization, the angular correlation function is more helpful than the angular power spectrum.

We are currently still unable to confirm the existence of k_{\min} with B -mode observations because there are no available data to use in the analysis. As we have shown above, however, if B -mode polarization is detected by the next-generation CMB missions, such as LiteBIRD, and the tensor-to-scalar ratio is not too far from its current upper limit, it should be possible to identify traces of k_{\min} in the B -mode data, especially in the angular correlation function. If B -mode polarization continues to elude detection, and the tensor-to-scalar ratio continues to decrease as the accuracy of detectors improves, it is possible that the value of r may fall below the threshold for us to detect k_{\min} . Of course, this does not mean k_{\min} does not exist; it merely means that when the tensor-to-scalar ratio is too small, as predicted by theory, the impact of k_{\min} on B -mode is not as pronounced as its effect on the temperature and E -mode signals.

2.6. Analysis of the $Q+U$ and $Q-U$ Modes

Up to this point, we have examined the impact of k_{\min} on the CMB’s temperature and polarization signals by calculating the theoretical predictions of the angular power spectrum

and angular correlation function for cases with and without this cutoff. And we then compared these results to the current *Planck* measurements, or described how the expected different outcomes could be used with future missions, such as LiteBIRD, to confirm or reject the existence of k_{\min} in the primordial power spectrum. This approach of calculating the angular correlation function is straightforward, as one can see in Equations (36) and (37).

Given the potential importance of identifying a non-zero k_{\min} to inflationary theory, we will next check these results by carrying out an independent analysis of the angular correlation function, based on an alternative approach. In this section, we adopt the method used by CAMB and, following CAMB's convention, refer to these angular correlation functions as the $Q+U$ mode and $Q-U$ mode (Lewis et al. 2000). Note, however, that they are not simply the sum or subtraction of the Q and U modes.

As we discussed earlier, the Q and U modes are ill-defined when viewed on the entire celestial sphere, because Q and U represent the linear polarization components along two orthogonal directions, and such a representation is not unique or invariant in a spherical coordinate system (Zaldarriaga & Seljak 1997). Different points on the sphere have different local coordinate systems, causing the direction of linear polarization to change with position. This makes it difficult to define consistent Q and U modes across the entire sky. Additionally, Q and U components mix with each other under coordinate system rotation, further complicating their definition on the sphere.

However, by using the complex forms of the polarization components, $Q+iU$ and $Q-iU$, this problem can be overcome. As we already explained earlier, this complex form of representation is known as spin-weighted fields, where $Q+iU$ is a spin +2 field and $Q-iU$ is a spin -2 field. Spin-weighted fields are rotationally invariant in the spherical coordinate system, meaning that when the coordinate system rotates, the change in the spin-weighted field is represented only by a phase factor, rather than a mixing of components. Therefore, using $Q+iU$ and $Q-iU$ allows for consistent polarization modes to be defined across the entire celestial sphere, which is particularly effective in CMB polarization analysis. The $Q+U$ and $Q-U$ modes we introduced here are actually $Q+iU$ and $Q-iU$ modes.

To compute the angular correlation function, we use the spin-weighted spherical harmonics, which naturally incorporate the rotational properties of the celestial sphere. For example, the angular correlation function $C_{Q+U}(\theta)$ is given by (NG & LIU 1999)

$$C_{Q+U}(\theta) = \sum_{\ell} \sqrt{\frac{2\ell+1}{4\pi}} (C_{\ell}^{EE} + C_{\ell}^{BB}) {}_2Y_{\ell}^{-2}(\theta, 0). \quad (38)$$

Similarly, the angular correlation function $C_{Q-U}(\theta)$ is

$$C_{Q-U}(\theta) = \sum_{\ell} \sqrt{\frac{2\ell+1}{4\pi}} (C_{\ell}^{EE} - C_{\ell}^{BB}) {}_2Y_{\ell}^2(\theta, 0). \quad (39)$$

In the CAMB software, these angular correlation functions are computed using the Wigner d-functions $d_{22}(\theta)$ and $d_{2,-2}(\theta)$. Specifically, CAMB uses the following formulas to compute the polarization correlation functions (Lewis et al. 2000):

$$\begin{aligned} C_{Q+U}(\theta) &= \sum_{\ell=2}^{\ell_{\max}} \left(\frac{2\ell+1}{4\pi} \right) (C_{\ell}^{EE} + C_{\ell}^{BB}) d_{2,2}(\theta), \\ C_{Q-U}(\theta) &= \sum_{\ell=2}^{\ell_{\max}} \left(\frac{2\ell+1}{4\pi} \right) (C_{\ell}^{EE} - C_{\ell}^{BB}) d_{2,-2}(\theta). \end{aligned} \quad (40)$$

In CAMB's calculations, the Wigner d -functions are generated from the following equations:

$$\begin{aligned} d_{2,2} &= \frac{[(4x-8) + \ell(\ell+1)] P_{\ell}(x) + 4 \left(\frac{1-x}{1+x} \right) (1+x)}{(\ell+2)(\ell-1)} \\ &\quad + \frac{4 \left(\frac{1-x}{1+x} \right) \left(\frac{x-2}{\ell(\ell+1)} \right) P'_{\ell}(x)}{(\ell+2)(\ell-1)}, \\ d_{2,-2} &= \frac{[\ell(\ell+1) - (4x+8)] P_{\ell}(x) + 4 \left(\frac{1+x}{1-x} \right) (-1-x)}{(\ell+2)(\ell-1)} \\ &\quad + \frac{4 \left(\frac{1+x}{1-x} \right) \left(\frac{x+2}{\ell(\ell+1)} \right) P'_{\ell}(x)}{(\ell+2)(\ell-1)}, \end{aligned}$$

where x stands for $\cos(\theta)$. These formulas leverage the properties of the Wigner d -functions to ensure accurate and efficient computation of the angular correlation function, taking into account the spin-2 nature of the polarization fields.

The results of these calculations are shown in Figures 12 and 13. In both cases, the red curve represents the theoretical prediction without k_{\min} , while the blue curve shows outcome with a non-zero k_{\min} . The results calculated from *Planck*'s data are shown in green along with their 1σ error region. For both sets of plots, we selected the range of multipoles to be $\ell < 30$, because k_{\min} affects only the low- ℓ region of C_{ℓ} . Additionally, including high- ℓ terms of C_{ℓ} makes the angular correlation function fuzzy. Thus, selecting this range allows us to better gauge the impact of k_{\min} .

All the theoretical curves in these two plots were calculated entirely with CAMB. Specifically, the theoretical prediction of the angular correlation function shown here is calculated from the angular power spectrum produced by CAMB. During this process, the most updated parameters (Planck Collaboration et al. 2020a) from *Planck* were used. The *Planck* measurements shown in these figures were derived through three thousand steps of Monte Carlo (MC) simulations. Specifically, we took the *Planck* measurements of

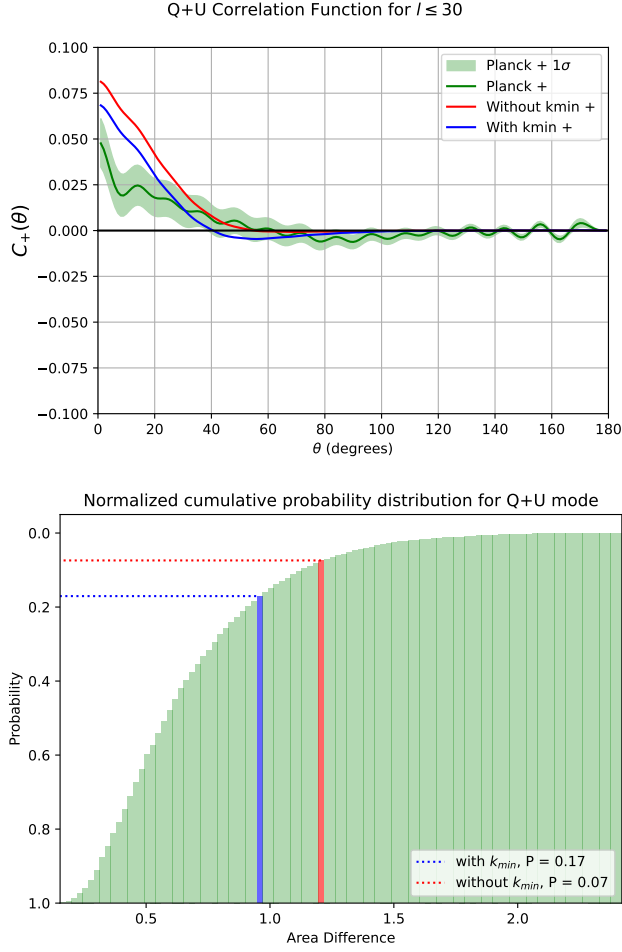


Figure 12. $Q+U$ angular correlation function. Top: the $Q+U$ angular correlation function including $\ell \leq 30$ modes. The blue curve includes the effects of k_{\min} , while the red curve represents calculations without k_{\min} , i.e., the conventional application of the standard model. The green curve represents the angular correlation function calculated from the *Planck*-2018 data. The corresponding 1σ region was generated from a three thousand step MC simulation utilizing the total errors in *Planck*'s measurements. Bottom: The cumulative probability distribution of the $Q+U$ mode, generated from the area differences between the *Planck* curve and the three thousand realizations mentioned above, which were produced using *Planck*'s total errors. Blue represents the model with k_{\min} ; red represents the model without k_{\min} .

the E -mode angular power spectrum along with their total errors. We then randomized these C_ℓ 's into three thousand sets of mock C_ℓ 's. For each set of C_ℓ 's, we calculated an angular correlation function using CAMB. We then calculated the mean and the standard deviation of the angular correlation function at each angle. One point to stress is that the evaluation of the $Q+U$ and $Q-U$ angular correlation functions requires both the C_ℓ^{EE} 's and C_ℓ^{BB} 's. *Planck* only has E -mode measurements, however. But since the tensor-to-scalar ratio has already been constrained to a very small value, $r < 0.036$,

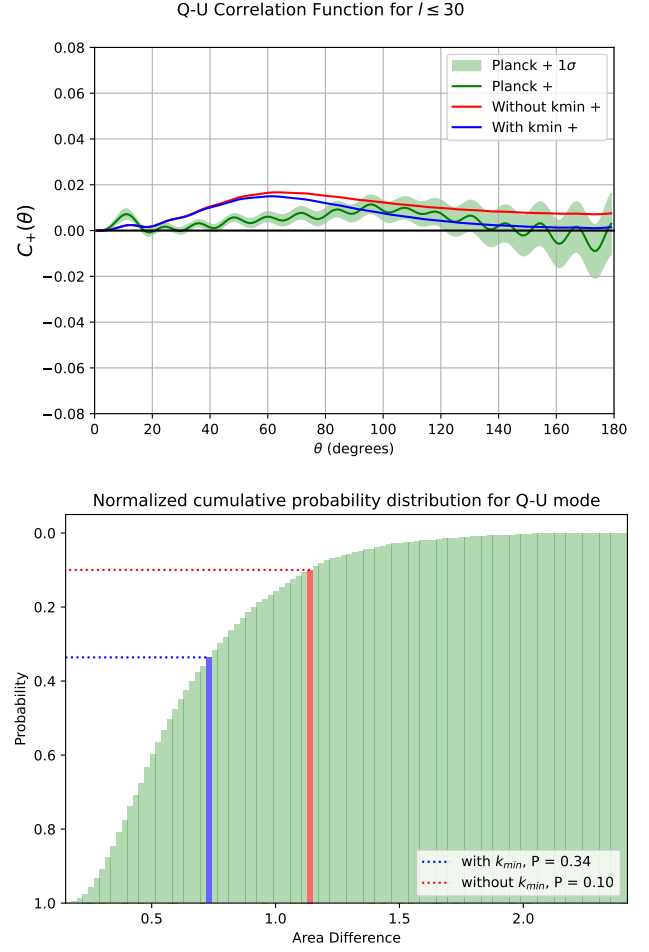


Figure 13. $Q-U$ angular correlation functions. Top: the $Q-U$ angular correlation function including $\ell \leq 30$ modes. The blue curve includes the effects of k_{\min} , while the red curve represents calculations without k_{\min} , i.e., the conventional application of the standard model. The green curve represents the angular correlation function calculated from the *Planck*-2018 data. The corresponding 1σ region was generated from a three thousand step MC simulation utilizing the total errors in *Planck*'s measurements. Bottom: The cumulative probability distribution of the $Q-U$ mode, generated from the area differences between the *Planck* curve and the three thousand realizations mentioned above, which were produced using *Planck*'s total errors. Blue represents the model with k_{\min} ; red represents the model without k_{\min} .

using only the E -mode angular power spectrum in these calculations is a very good approximation. Therefore, for both the theoretical predictions and the *Planck* measurements, we used only the E -mode angular power spectrum.

The $Q+U$ mode angular correlation function is plotted in Figure 12. The top panel shows the results of the calculation using the C_ℓ 's within the range $\ell \leq 30$. As we can see from the plot, both theoretical curves fit the measurements very poorly and both miss the 1σ error region of the measurements at $\theta < 20$ degrees. It is still clear, however, that

introducing k_{\min} brings the theoretical predictions closer to the measurements.

The $Q-U$ mode angular correlation function is plotted in Figure 13. The top panel shows the results of the calculation using the C_ℓ 's within the range $\ell \leq 30$. Although both theoretical curves fail to fit the measurements very well at $\theta < 60$ degrees, the prediction with k_{\min} fits the measurements quite well at $\theta > 80$ degrees, whereas the curve without k_{\min} fails significantly at all angles, it falls outside the 1σ error region of the measurement at almost all angles.

Analogously to the E -mode correlation and the TE cross-correlation, we use a cumulative probability approach to estimate the likelihood that the area difference between a theoretical curve and the *Planck* curve arises solely from the total errors of the *Planck* measurements. The cumulative probability distribution plot of the $Q+U$ mode is presented in the bottom panel of Figure 12. The cumulative probability distribution plot of the $Q-U$ mode is presented in the bottom panel of Figure 13.

The results are as follows: For the $Q+U$ mode, in the case without k_{\min} , the probability that the area difference is due to the total errors of the *Planck* measurements is 0.07. In the case with k_{\min} , the probability is 0.17. For the $Q-U$ mode, in the case without k_{\min} , the probability is 0.10. In the case with k_{\min} , the probability is 0.34.

These results for the $Q+U$ and $Q-U$ angular correlation functions clearly confirm the findings of previous studies and the results presented earlier in this paper. In both cases, introducing k_{\min} helps bring the theoretical predictions closer to the measurements. This is especially true in the $Q-U$ case, in which the difference between the models with and without k_{\min} is significant, and the one with k_{\min} is a much better fit to the data. These results favor the model with k_{\min} and thus add to the justification for the existence of k_{\min} .

3. CONCLUSION

The hypothesized delayed initiation of inflation would produce a rigid cut-off, k_{\min} , for both the scalar and tensor primordial power spectra (Liu & Melia 2020; Liu & Melia 2024a). This will impact all aspects of the CMB observations, including the temperature and polarization signals. *Planck* has conducted precise measurements of the temperature fluctuations and the E -mode polarization (Planck Collaboration et al. 2020a). B -mode polarization, however, has not been detected yet. One can anticipate that the next-generation missions, such as LiteBIRD, will be capable of detecting the B -mode and finally determine the tensor-to-scalar ratio, r (LiteBIRD Collaboration et al. 2023). In this paper, we have calculated the theoretical predictions of the angular power spectrum and the angular correlation function for both cases, with and without k_{\min} . And we have compared the theoretical predictions with the available measure-

ments. For the B -mode, we compared the differences in the expected fits with and without k_{\min} , and discussed the possibility that LiteBIRD may be able to distinguish between these two cases, depending on the value of r .

Based on our analysis, the existence of k_{\min} is already on firm ground. Its introduction significantly helps to align the theoretical predictions with the existing data. Our analysis not only confirms the results obtained in earlier studies (Melia & López-Corredoira 2018; Melia et al. 2021), based primarily on the temperature signal, but goes further in providing even stronger evidence for a non-zero cutoff to the primordial power spectrum.

Specifically, the introduction of k_{\min} enhances the theoretical fit of the E -mode polarization. The improvement is noticeable in both the angular power spectrum and the angular correlation function, for which the theoretical curves with k_{\min} fit the *Planck* data more closely compared to the standard model without the cutoff.

The TE cross-correlation function analysis further supports the impact of k_{\min} . Its inclusion in the model reduces discrepancies between the theoretical predictions and the data across various angles, thereby easing tensions observed in the standard model.

Although current B -mode observations are very limited, our analysis indicates that k_{\min} affects the B -mode angular power spectrum and angular correlation function in measurable ways. The difference between models with and without k_{\min} is more pronounced at low multipoles, however, so that ought to be an important focus of upcoming observations, particularly if the tensor-to-scalar ratio r is not too much smaller than its current upper limit.

We have also confirmed these results with a separate analysis based on the use of the $Q+U$ and $Q-U$ angular correlation functions, which fully support the conclusion that introducing k_{\min} mitigates the tension between the observations and the current suite of theoretical predictions. This is especially evident in the $Q-U$ case, where the difference between the fits with and without k_{\min} is significant.

For all the cases (TT , EE , TE , $Q+U$, and $Q-U$) where we have calculated the angular correlation function of the predictions and the *Planck* measurements, we compared the two models (with and without k_{\min}) using a cumulative probability distribution plot. In all cases, the model with k_{\min} shows a much higher likelihood that the discrepancy between theory and measurements is solely due to the total errors of the measurements. In other words, the model with k_{\min} is favored in all cases.

In conclusion, our comprehensive analysis across temperature, E -mode, TE cross-correlation, and B -mode polarization signals robustly supports the introduction of k_{\min} in the primordial power spectrum. This cutoff not only helps resolve the large-angle anomalies observed in the CMB, but also pro-

vides a more accurate representation of the early Universe’s inflationary epoch. Future observations, particularly of the

B -mode polarization, will be crucial for further validating the existence and implications of k_{\min} .

- ¹ FM is grateful to Amherst College for its support through a
- ² John Woodruff Simpson Fellowship.

REFERENCES

- Ade, P. A. R., Ahmed, Z., Amiri, M., et al. 2021, *PhRvL*, 127, 151301, doi: [10.1103/PhysRevLett.127.151301](https://doi.org/10.1103/PhysRevLett.127.151301)
- Barvinsky, A. O., Kamenshchik, A. Y., & Starobinsky, A. A. 2008, *JCAP*, 2008, 021, doi: [10.1088/1475-7516/2008/11/021](https://doi.org/10.1088/1475-7516/2008/11/021)
- Baumann, D., & Zaldarriaga, M. 2009, *Journal of Cosmology and Astroparticle Physics*, 2009, 013, doi: [10.1088/1475-7516/2009/06/013](https://doi.org/10.1088/1475-7516/2009/06/013)
- Bennett, C. L., Hill, R. S., Hinshaw, G., et al. 2003, *ApJS*, 148, 97, doi: [10.1086/377252](https://doi.org/10.1086/377252)
- Bezrukov, F., & Shaposhnikov, M. 2008, *Physics Letters B*, 659, 703, doi: [10.1016/j.physletb.2007.11.072](https://doi.org/10.1016/j.physletb.2007.11.072)
- Contaldi, C. R., Peloso, M., Kofman, L., & Linde, A. 2003, *JCAP*, 2003, 002, doi: [10.1088/1475-7516/2003/07/002](https://doi.org/10.1088/1475-7516/2003/07/002)
- Copi, C. J., Huterer, D., Schwarz, D. J., & Starkman, G. D. 2010, *Advances in Astronomy*, 2010, 847541, doi: [10.1155/2010/847541](https://doi.org/10.1155/2010/847541)
- Cruz, M., Martínez-González, E., Vielva, P., & Cayón, L. 2005, *Monthly Notices of the Royal Astronomical Society*, 356, 29, doi: [10.1111/j.1365-2966.2004.08419.x](https://doi.org/10.1111/j.1365-2966.2004.08419.x)
- Eriksen, H. K., Hansen, F. K., Banday, A. J., Górski, K. M., & Lilje, P. B. 2004, *The Astrophysical Journal*, 605, 14, doi: [10.1086/382267](https://doi.org/10.1086/382267)
- Gorski, K. M., Hivon, E., Banday, A. J., et al. 2005, *The Astrophysical Journal*, 622, 759–771, doi: [10.1086/427976](https://doi.org/10.1086/427976)
- Guth, A. H. 1981, *PhRvD*, 23, 347, doi: [10.1103/PhysRevD.23.347](https://doi.org/10.1103/PhysRevD.23.347)
- Hazra, D. K., Shafieloo, A., Smoot, G. F., & Starobinsky, A. A. 2014, *Journal of Cosmology and Astroparticle Physics*, 2014, 048, doi: [10.1088/1475-7516/2014/08/048](https://doi.org/10.1088/1475-7516/2014/08/048)
- Hinshaw, G., Banday, A. J., Bennett, C. L., et al. 1996, *ApJL*, 464, L25, doi: [10.1086/310076](https://doi.org/10.1086/310076)
- Ijjas, A., Steinhardt, P. J., & Loeb, A. 2013, *Physics Letters B*, 723, 261, doi: [10.1016/j.physletb.2013.05.023](https://doi.org/10.1016/j.physletb.2013.05.023)
- . 2014, *Physics Letters B*, 736, 142, doi: [10.1016/j.physletb.2014.07.012](https://doi.org/10.1016/j.physletb.2014.07.012)
- Kazanas, D. 1980, *ApJL*, 241, L59, doi: [10.1086/183361](https://doi.org/10.1086/183361)
- Kolb, E. W., & Turner, M. S. 1994, *The Early Universe* (Oxford: Taylor and Francis), doi: [10.1201/9780429492860](https://doi.org/10.1201/9780429492860)
- Kosowsky, A. 1996, *Annals of Physics*, 246, 49, doi: [https://doi.org/10.1006/aphy.1996.0020](https://doi.org/https://doi.org/10.1006/aphy.1996.0020)
- Lee, H. M. 2018, *PhRvD*, 98, 015020, doi: [10.1103/PhysRevD.98.015020](https://doi.org/10.1103/PhysRevD.98.015020)
- Lewis, A., & Challinor, A. 2006, *PhR*, 429, 1, doi: [10.1016/j.physrep.2006.03.002](https://doi.org/10.1016/j.physrep.2006.03.002)
- Lewis, A., Challinor, A., & Lasenby, A. 2000, *ApJ*, 538, 473, doi: [10.1086/309179](https://doi.org/10.1086/309179)
- Liddle, A. R. 1994, *PhRvD*, 49, 739, doi: [10.1103/PhysRevD.49.739](https://doi.org/10.1103/PhysRevD.49.739)
- Linde, A. D. 1982, *Physics Letters B*, 108, 389, doi: [10.1016/0370-2693\(82\)91219-9](https://doi.org/10.1016/0370-2693(82)91219-9)
- . 1983, *Physics Letters B*, 129, 177, doi: [10.1016/0370-2693\(83\)90837-7](https://doi.org/10.1016/0370-2693(83)90837-7)
- LiteBIRD Collaboration, Allys, E., Arnold, K., et al. 2023, *Progress of Theoretical and Experimental Physics*, 2023, 042F01, doi: [10.1093/ptep/ptac150](https://doi.org/10.1093/ptep/ptac150)
- Liu, J., & Melia, F. 2020, *Proceedings of the Royal Society of London Series A*, 476, 20200364, doi: [10.1098/rspa.2020.0364](https://doi.org/10.1098/rspa.2020.0364)
- Liu, J., & Melia, F. 2024a, *The Astrophysical Journal*, 967, 109, doi: [10.3847/1538-4357/ad4036](https://doi.org/10.3847/1538-4357/ad4036)
- . 2024b, *Phys. Lett. B*, 853, 138645, doi: [10.1016/j.physletb.2024.138645](https://doi.org/10.1016/j.physletb.2024.138645)
- Ma, C.-P., & Bertschinger, E. 1995, *ApJ*, 455, 7, doi: [10.1086/176550](https://doi.org/10.1086/176550)
- Martin, J., & Brandenberger, R. H. 2001, *PhRvD*, 63, 123501, doi: [10.1103/PhysRevD.63.123501](https://doi.org/10.1103/PhysRevD.63.123501)
- Melia, F. 2022, *Astronomische Nachrichten*, 343, e24010, doi: [10.1002/asna.20224010](https://doi.org/10.1002/asna.20224010)
- . 2023a, *Physics of the Dark Universe*, 42, 101329, doi: [10.1016/j.dark.2023.101329](https://doi.org/10.1016/j.dark.2023.101329)
- . 2023b, *Annalen der Physik*, 535, 2300157, doi: [10.1002/andp.202300157](https://doi.org/10.1002/andp.202300157)
- Melia, F., & López-Corredoira, M. 2018, *A&A*, 610, A87, doi: [10.1051/0004-6361/201732181](https://doi.org/10.1051/0004-6361/201732181)
- Melia, F., Ma, Q., Wei, J.-J., & Yu, B. 2021, *A&A*, 655, A70, doi: [10.1051/0004-6361/202141251](https://doi.org/10.1051/0004-6361/202141251)
- Melia, F., & Yennapureddy, M. K. 2018, *JCAP*, 2018, 034, doi: [10.1088/1475-7516/2018/02/034](https://doi.org/10.1088/1475-7516/2018/02/034)
- Mukhanov, V. F., Feldman, H. A., & Brandenberger, R. H. 1992, *PhR*, 215, 203, doi: [10.1016/0370-1573\(92\)90044-Z](https://doi.org/10.1016/0370-1573(92)90044-Z)
- NG, K.-W., & LIU, G.-C. 1999, *International Journal of Modern Physics D*, 08, 61–83, doi: [10.1142/s0218271899000079](https://doi.org/10.1142/s0218271899000079)
- Planck Collaboration, Ade, P. A. R., Aghanim, N., et al. 2014, *A&A*, 571, A16, doi: [10.1051/0004-6361/201321591](https://doi.org/10.1051/0004-6361/201321591)

- Planck Collaboration, Aghanim, N., Akrami, Y., et al. 2020a, A&A, 641, A6, doi: [10.1051/0004-6361/201833910](https://doi.org/10.1051/0004-6361/201833910)
- Planck Collaboration, Akrami, Y., Ashdown, M., et al. 2020b, A&A, 641, A7, doi: [10.1051/0004-6361/201935201](https://doi.org/10.1051/0004-6361/201935201)
- Sanchis-Lozano, M. A., Melia, F., López-Corredoira, M., & Sanchis-Gual, N. 2022, A&A, 660, A121, doi: [10.1051/0004-6361/202142296](https://doi.org/10.1051/0004-6361/202142296)
- Schwarz, D. J., Copi, C. J., Huterer, D., & Starkman, G. D. 2016, Classical and Quantum Gravity, 33, 184001, doi: [10.1088/0264-9381/33/18/184001](https://doi.org/10.1088/0264-9381/33/18/184001)
- Seljak, U., & Zaldarriaga, M. 1996, ApJ, 469, 437, doi: [10.1086/177793](https://doi.org/10.1086/177793)
- Starobinskiĭ, A. A. 1979, Soviet Journal of Experimental and Theoretical Physics Letters, 30, 682
- Tristram, M., Banday, A. J., Górski, K. M., et al. 2021, A&A, 647, A128, doi: [10.1051/0004-6361/202039585](https://doi.org/10.1051/0004-6361/202039585)
- Yoho, A., Copi, C. J., Starkman, G. D., & Kosowsky, A. 2014, Monthly Notices of the Royal Astronomical Society, 442, 2392–2397, doi: [10.1093/mnras/stu942](https://doi.org/10.1093/mnras/stu942)
- Zaldarriaga, M., & Seljak, U. 1997, PhRvD, 55, 1830, doi: [10.1103/PhysRevD.55.1830](https://doi.org/10.1103/PhysRevD.55.1830)
- Zaldarriaga, M., & Seljak, U. 1998, Physical Review D, 58, doi: [10.1103/physrevd.58.023003](https://doi.org/10.1103/physrevd.58.023003)